Forefront of Modelings, Measurements, and Machine Learnings of Hydro-environmental Flows

Longitudinal Change in Flow Structures and Energy Loss of Free Jumps and Submerged Jumps of Flows over an Embankment-type Weir

Seongwook Choi[a] and Sung-Uk Choi [b]

[a]Dept. of Civil and Environmental Engineering, Yonsei University, Seoul 03722, Korea
[b]Dept. of Civil and Environmental Engineering, Yonsei University, Seoul 03722, Korea

ABSTRACT

This study numerically investigates the longitudinal changes in the flow structures and energy loss of the free jumps and the submerged jumps. The hydraulic jumps from flows over an embankment-type weir are considered. For the numerical simulations, the 2D Unsteady Reynolds-Averaged Navier-Stokes equations are solved using the $k-\omega$ SST turbulence model. Flow structures and their longitudinal changes are compared with the available experimental data, showing moderate agreement. The simulation results indicate that the decaying patterns of the flow structures for the free jump are roughly similar to those for the submerged jump. The decaying rate decreases with increasing submergence ratio, in which process the adverse pressure gradient plays a key role. It is also confirmed that the loss of the kinetic energy increases with decreasing submergence ratio. For both free jump and submerged jump, the process of dissipating the kinetic energy terminates within the developed zone, with the decaying process of the flow structure unfinished.

1. Introduction

The flows over an embankment-type weir exhibit various flow types depending on the tailwater depth far downstream of the weir (see Fig. 1). For low flows, a hydraulic jump occurs downstream from the toe of the weir. This is called a "swept-out jump." As the tailwater depth rises, the sequent depth before the jump decreases, moving the front of the jump in the upstream direction. A hydraulic jump that occurs right at the toe of the weir is called an "optimum jump." The term "free jump" refers to both the swept-out jump and the optimum jump. If the tailwater depth further increases, then the toe of the jump is covered by the downstream water, resulting in a "submerged jump." A further increase in the tailwater depth leads to a "washed-out jump" with standing waves on the water surface.

Among the four flow types, free jumps and submerged jumps are of particular interest in engineering practice. The optimum jump is known to have the best efficiency in energy dissipation. For the swept-out jump, since the flow depth increases on the horizontal bed after passing the toe of the weir, the difference in the flow depths before and after the jump decreases, according to

Belanger equation. This leads to less energy dissipation for the swept-out jump compared with the optimum jump. For the free jump, the flow accelerates, and thus, the flow depth decreases along the downslope of the weir. However, for the submerged jump, the flow decelerates after plunging, and the flow depth increases by entraining air and water from the upper recirculating region. This results in less energy dissipation for the submerged jump compared with the free jump.

In general, for both free jumps and submerged jumps, the flow regime can be divided into four regions (see Fig. 2). First, the supercritical flow before the jump constitutes the developing zone. For the submerged jump, the flow in this zone resembles the potential core of a wall jet. The developing zone is followed by the developed zone. For both free jumps and submerged jumps, the developed zone consists of two regions in the vertical direction, the wall-jet region near the bed and the roller region above the wall-jet region. A shear layer exists between the two regions, and this shear layer strongly affects the flow in the developed zone. The flow in the developed zone is affected by the adverse pressure gradient, which is true for both free jumps and submerged jumps. The end of the developed zone is connected
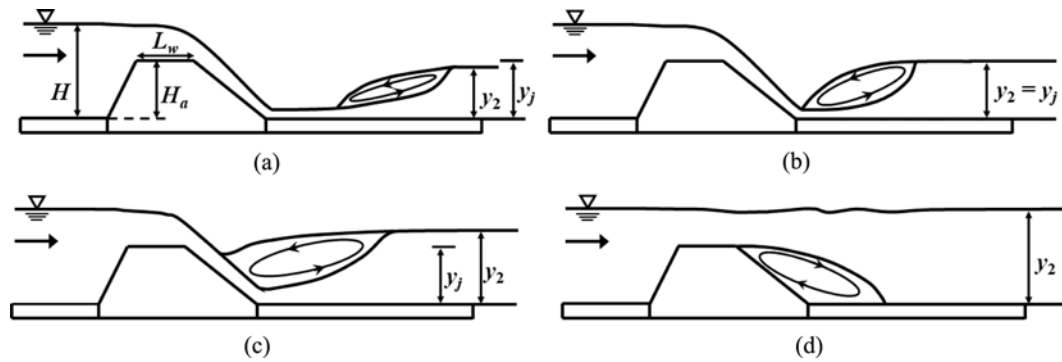
Fig. 1. Transition of Flow over an Embankment-Type Weir: (a) Swept-Out Hydraulic Jump, (b) Optimum Hydraulic Jump, (c) Submerged Hydraulic Jump, (d) Washed-Out Hydraulic Jump
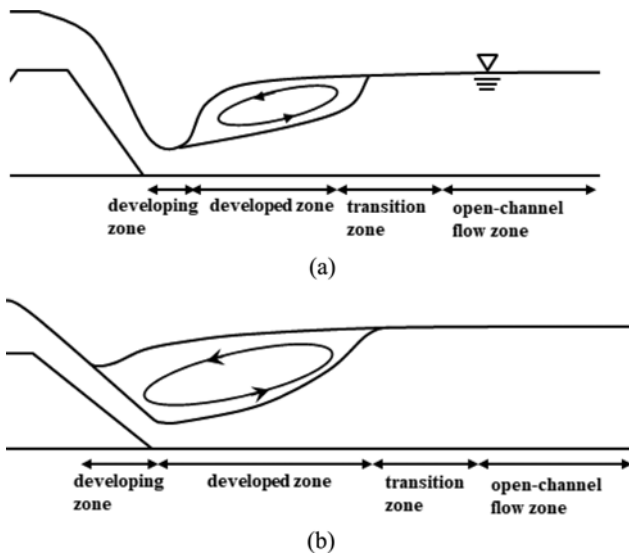

Fig. 2. Different Zones of Hydraulic Jumps: (a) Free Jump, (b) Submerged Jump

to the transition zone, which extends from the end of the roller to the distance where the flow recovers to the open-channel flow. For the free jump whose inflow Froude number (Fr_1) is between 3.9 and 10.5, the length of the transition zone is about 10 times that of the tailwater depth (Wu and Rajaratnam, 1996). The last region is the open-channel flow zone. In this zone, the flow structures recover to those of the open-channel flow, which is not affected by the re-circulating flows, and the pressure becomes hydrostatic.

The submerged jump, which creates an extended roller with strong re-circulating flows, is most dangerous due to the extraordinarily calm water surface. Since the body of the submerged jump is not directly exposed to air, air entrainment is known to be much less than that of the free jump. Experiments have shown that submerged jumps induce much smaller pressure fluctuations on the bed than free jumps (Narasimhan and Bhargava, 1976). The energy loss by the submerged jump, a function of the inflow Froude number and submergence factor, is known to be less than that by the free jump (Hager, 1992; Pourabdollah et al., 2020). However, it is difficult to estimate the energy loss of the

submerged jump because formulas, such as the Belanger equation for the free jump, are not applicable to the submerged jump. The energy loss can roughly be estimated by comparing specific energies before and after the jump (Pourabdollah et al., 2020), which is not an easy task either in the laboratory or in the field.

Previous studies have explored the mean flow and turbulence statistics of the free jump and submerged jump using laboratory experiments and numerical simulations. For example, Long et al. (1990) measured the flow structures of submerged jumps under a sluice gate using laser Doppler velocimetry. Wu and Rajaratnam (1995) measured the vertical velocity profiles of submerged jumps under a sluice gate. Fritz and Hager (1998) performed laboratory experiments on flows over an embankment weir. Liu et al. (2004) measured the turbulence structure of free jumps with low inflow Froude numbers (Fr_1 = 2.0, 2.5, and 3.32) using MicroADV. Jesudhas et al. (2017) presented the vertical profiles of the mean velocity and Reynolds stress and coherent structures of submerged jumps under the sluice gate using the detached eddy simulation. A similar study on free jumps was also carried out by Jesudhas et al. (2018). These studies suggest that the flow structures of the free jump decay faster than those of the submerged jump. This is thought to be related to the efficiency of the energy dissipation capacity of the free jump. However, how and why the flow structures of free jumps decay fast in the longitudinal direction compared with submerged jumps has not been demonstrated. Moreover, there is a dearth of studies that have investigated the relationship between the decay of flow structures and energy loss.

The objective of this study is to explore the longitudinal changes in the flow structures and how they are related to the longitudinal dissipation of the mean kinetic energy for the free jump and submerged jumps using numerical simulations. The free jump and submerged jumps of the flows over an embankment-type weir are considered. The 2D Unsteady Reynolds-Averaged Navier-Stokes (URANS) equations are solved with the k–ω SST turbulence model using the open source platform OpenFOAM (Jasak, 2009). Model validations are carried out by comparing computed results with measured data for a free jump case in the literature. For a fixed unit discharge, a free jump and three submerged jumps with various values of the submergence factor,

ranging from 0.5 to 0.88, are reproduced by changing the tailwater depth. Flow structures, such as streamwise mean velocity, turbulence intensity, Reynolds stress, and mean pressure, are presented, followed by decays of the flow structures of the free jump and submerged jumps. The similarities in the decay of the flow structures between the free jump and the submerged jumps are also investigated. Lastly, the change in the energy loss with distance is given and considered together with the change in the flow structures.

2. Numerical Model

2.1 Governing Equations and Turbulence Model

The following URANS equations are solved to compute the flows over the weir:

$$\frac{\partial \rho}{\partial t} + \frac{\partial \rho \tilde{u}_i}{\partial x_i} = 0 \,, \tag{1}$$

$$\frac{\partial \rho \tilde{u}_i}{\partial t} + \frac{\partial \rho \tilde{u}_i \tilde{u}_j}{\partial x_j} = -\frac{\partial \tilde{p}}{\partial x_i} + \frac{1}{\partial x_j}\left\{ (\mu + \mu_t)\left(\frac{\partial \tilde{u}_i}{\partial x_j} + \frac{\partial \tilde{u}_j}{\partial x_i} \right) \right\} + \rho g_i \,, \tag{2}$$

where x_i is the Cartesian axis direction (i = 1, 2), $\tilde{u}_i$ is the ensemble-averaged velocity in the x_i direction, t is the time, ρ is the density of the water-air mixture, $\tilde{p}$ is the ensemble-averaged pressure, μ is the viscosity of the water-air mixture, μ_t is the turbulent viscosity, and g is the gravitational acceleration.

In the present study, the Volume of Fluid (VOF) method is used to predict the free surface (Hirt and Nichols, 1981). The VOF method, which is a widely-used Eulerian method for computing multiphase flows, is used to solve the transport equation of the volume fraction of water (α) such as

$$\frac{\partial \alpha}{\partial t} + \frac{\partial \alpha \tilde{u}_i}{\partial x_i} = 0 \,. \tag{3}$$

In general, the value of α is between 0 and 1, representing the states fully occupied by air and water, respectively. The VOF method solves the single momentum equation for multiphase flows, in which the viscosity and density of the water-air mixture are expressed in terms of α, respectively, as

$$\mu = \alpha \mu_{water} + (1-\alpha)\mu_{air} \,, \tag{4}$$

$$\rho = \alpha \rho_{water} + (1-\alpha)\rho_{air} \,, \tag{5}$$

where μ_{water} and μ_{air} are the dynamic viscosity of water and air, respectively, and ρ_{water} and ρ_{air} are the density of water and air, respectively.

The k–ω SST turbulence model was developed by Menter (1992) and has successfully been applied to predicting the flows with separations or stagnations under adverse pressure gradient (Kang et al., 2011; Khosronejad et al., 2015). The k–ω SST turbulence model estimates the turbulent viscosity μ_t in Eq. (2) by

$$\mu_t = \frac{a_1 \rho k}{\max(a_1 \omega, \overline{S}F_2)} \,, \tag{6}$$

where k is the turbulence kinetic energy, ω is the specific dissipation rate of k, $\overline{S}$ is the strain rate of the flow, a_1 is a model constant (= 0.31), and F_2 is a blending function. In the present study, the blending function proposed by Menter (1992) is adopted. To obtain k and ω, the following transport equations for k and ω are solved, respectively:

$$\frac{\partial k}{\partial t} + \tilde{u}_j \frac{\partial k}{\partial x_j} = \frac{1}{\partial x_j}\left\{ (\nu + \sigma_k \nu_t)\frac{\partial k}{\partial x_j} \right\} + P_k - \beta^* k\omega \,, \tag{8}$$

$$\frac{\partial \omega}{\partial t} + \tilde{u}_j \frac{\partial \omega}{\partial x_j} = \frac{1}{\partial x_j}\left\{ (\nu + \sigma_\omega \nu_t)\frac{\partial \omega}{\partial x_j} \right\} + \alpha_1 \overline{S}^2 - \beta\omega^2 + 2(1-F_1)\sigma_{\omega 2}\frac{1}{\omega}\frac{\partial k}{\partial x_i}\frac{\partial \omega}{\partial x_i} \,, \tag{9}$$

where ν is the kinematic viscosity of the water-air mixture, ν_t is the turbulent kinematic viscosity, P_k is the production term of k, σ_k, σ_ω, α_1, β^*, β, and $\sigma_{\omega 2}$ are the model coefficients, and F_1 is a blending function. The model coefficients σ_k, σ_ω, and β are obtained through the blending function F_1 such as

$$\phi = \phi_1 F_1 + (1-\phi_1)F_1 \,. \tag{10}$$

In the present study, the values of such coefficients as α_1 = 5/9, β^* = 9/100, β_1 = 3/40, β_2 = 0.0828, σ_{k1} = 0.85, σ_{k2} = 1, $\sigma_{\omega 1}$ = 0.5, and $\sigma_{\omega 2}$ = 0.856 are used (Menter, 1992).

To calculate the velocity-pressure coupling, interFoam in OpenFOAM based on the PISO algorithm and the SIMPLE algorithm is used. The time derivative terms are discretized using the Euler scheme. The convection and diffusion terms are discretized with the help of the Gauss vanLeer and the Gauss linear corrected scheme, respectively, in OpenFOAM. All discretized terms are interpreted using the generalized geometric-algebraic multi-grid (GAMG) matrix solver.

2.2 Boundary Conditions

The boundary conditions required for computing hydraulic jumps consist of the inlet, outlet, bed and weir, and the upper open air patch. The Dirichlet boundary condition is used at the inlet boundary. That is, the streamwise mean velocity from the log law is prescribed with the upstream flow depth. The pressure is hydrostatic with arbitrary small values for k and ω at the inlet boundary. The outlet boundary is a freefall, where the ensemble-averaged pressure is zero, that is, $\tilde{p}$ = 0. The no-slip boundary condition is used at the wall, and the wall functions are used for k and ω (Jasak, 2009). At the air-filled upper boundary of the solution domain, the ensemble-averaged pressure is set to zero.

3. Model Validation

In the present section, the numerical model is validated. Although the URANS model is indeed a feasible alternative for engineering computations at practical Reynolds numbers, as pointed out by Paik et al. (2009), the performance of the URANS model, especially, when applied to multi-phase flows such as hydraulic jumps, has not been fully proved. Herein, the numerical model is

used to compute a case of the free jump in laboratory experiments by Wang et al. (2014) for model validation. For measurements of air-water flows, Wang et al. used dual-tip phase-detection probes, from which signals show two distinctive peaks of air and water flows. They presented the turbulent properties of hydraulic jumps, such as turbulent intensity and integral scales.

The experimental case selected is the free jump with an inflow Froude number of 7.5. This corresponds to a steady jump, in which the location of the roller is rather fixed, according to the classification of hydraulic jumps in Chow (1959). The unit discharge is 0.0666 $m^2 s^{-1}$, and the flow depth and velocity before the jump are 0.02 m and 3.33 m s^{-1}, respectively. Here, for validation, the numerical model is applied only to the free jump because the free jump is more challenging for numerical simulations due to more air entrainment, compared with the submerged jump (Long et al., 1991).

For computations, approximately a total number of 1.2×10^5 grids are used. The height of the computational domain is set to be 20 times the flow depth at the toe of the jump y_1. In the vicinity of the bed, the maximum wall normal distance $z^+ (= zu_*/v)$ is set to be less than 5 (here, z = vertical distance from the wall and u_* = shear velocity).
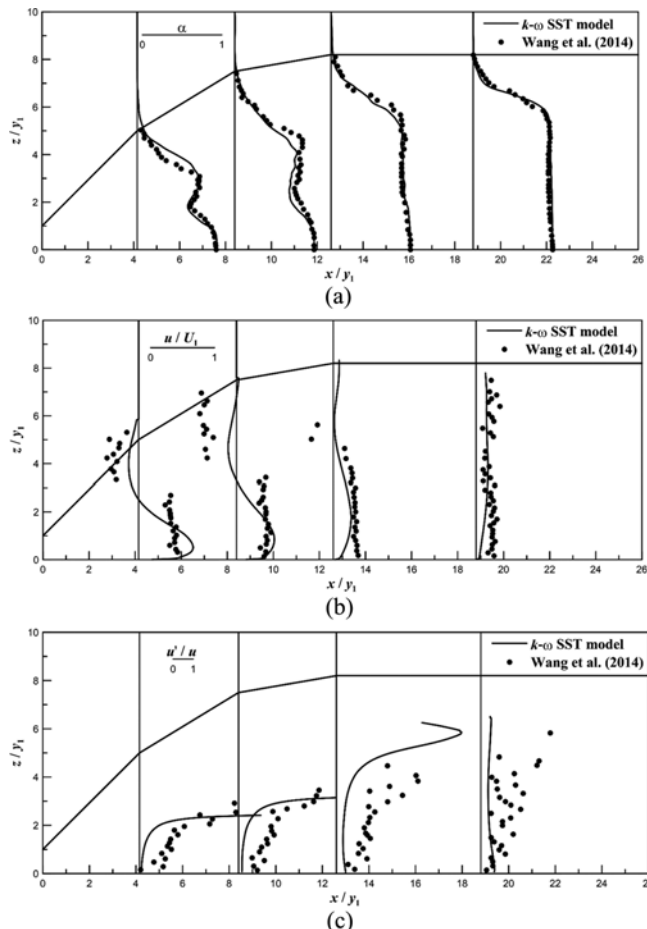

Figure 3(a) shows the vertical distributions of the volume fraction of water for the free jump at various longitudinal distances. Both the computed results and the measured data are provided for comparisons. A general trend observed in the figure is that the volume fraction of water, which is unity near the bed, decreases toward the free surface. The distributions in the developed zone, that is, at x/y_1 = 4.2 and 8.4, show a local minimum slightly below the interface between the wall-jet-like flow and the roller. Then, the volume fraction of water increases slightly, showing a local maximum within the roller, and decreases to zero toward the free surface. As shown in the figure, the computed results are in extremely good agreement with the measured data.

The distributions of the computed streamwise mean velocity are compared with the measured data in Fig. 3(b). For example, for $x / y_1 = 4.2$, the velocity profile shows a wall jet region for $0 < z / y_1 < 2.6$ and a backward flow region for $3.1 < z / y_1 < 5.2$, respectively. Both the computed results and measured data show longitudinal deceleration in the wall-jet region. However, the measured data in this region appear to be uniform in the vertical direction, unlike the computed results, which show a typical wall-jet-like flow, as measured by Lin et al. (2012). This is due to the use of dual-tip phase-detection probes, as discussed by Wang and Chanson (2015). The velocity in the backward flow region computed by the numerical model is found to be under-predicted compared with the measured data. This can be attributed to the fact that the computed velocity, in general, is less than the measured data in the backward flow region (Long et al., 1991; Javan and Eghbalzadeh, 2013) because the velocity by the VOF method corresponds to the velocity of the water-air mixture.

Figure 3(c) shows the distributions of the turbulence intensity at some longitudinal distances. The turbulence intensity u' is normalized by $\bar{u}(x, z)$. The normalized turbulence intensity, which is zero near the bed, increases from the bed and becomes very large or infinitely abruptly at a height, where $\bar{u} = 0$. The computed turbulence intensity shows a trend similar to that of the measured data but seems to be under-predicted. The difference between the computed results and the measured data can be attributed to Wang et al.'s (2014) method of estimating the turbulence intensity and the errors associated with the measurement of the mean velocity.

4. Applications

4.1 Flow Condition and Weir Dimension

In the present study, the flow conditions in Fritz and Hager's (1998) experiments are used to simulate the free jump and

Fig. 3. Model Validation: (a) Volume Fraction of Water, (b) Streamwise Mean Velocity, (c) x-Component Turbulence Intensity

Table 1. Dimension of Weir and Flow Conditions

Type	q (m^2/s)	H (m)	L_w (m)	H_a (m)	y_2 (m)	Fr_1	S
Free jump	0.055	0.4	0.3	0.3	0.17	3.85	0
Submerged jump					0.247	2.99	0.5
Submerged jump					0.303	2.18	0.77
Submerged jump					0.322	1.75	0.88

submerged jumps numerically with the k–ω SST turbulence model. Table 1 lists the flow conditions for the free jump and submerged jumps and the dimensions of the weir. In the table, H_a and L_w denote the weir height and crest length, respectively. The inflow Froude number Fr_1 for the free jump is 3.85, which suggests an oscillating jump (Chow, 1959). The flow condition and the dimension of the weir result in a relative embankment length of 0.25 ($= (H - H_a)/(H - H_a + L_w)$), indicating a broad-crested weir (here, H is the upstream flow depth). For a fixed unit discharge of 0.055 m^2 s^{-1}, a free jump and submerged jumps are reproduced by varying the tailwater depth. For the submerged jumps, the submergence factor $S (= (y_2 - y_j)/y_2)$ ranges between 0.5 and 0.88. For the bed roughness downstream from the toe of the weir, the hydraulically-smooth bed condition is used (W. H. Hager, personal communication, May 26, 2020).

4.2 Computational Grid

Table 2 lists the characteristic dimensions of the grid used in the present study. For efficient computations, unstructured grids of different local densities are used as shown in the figure below Table 2. The computational domain is divided into five subdomains. In the longitudinal direction, the computational domain extends 8H upstream and 25H downstream from the weir. The height of the computational domain is set to be greater than twice the tailwater depth so that the boundary condition at the top of the domain would not affect the water surface. The number of grids is approximately 1.4×10^5, and the grid size is chosen based on grid dependency tests, similar to Gumus et al. (2016). The detailed number of grids in the subdomain, near-wall grid size, and maximum wall normal distance z^+ in each subdomain are presented in the table. In general, fine grids are used in the region close to the bed and the free surface. Coarse and fine grids are used in the air and the roller regions, respectively. This results in a wall-normal distance z^+ less than 8.3 in Subdomain II, 4.31 at the toe of the weir in Subdomain III, and less than unity in the transition zone and open-channel flow zone.

The computational time step varies during the simulation. The

Table 2. Characteristic Dimensions of the Grid

Subdomain*	Element number	Near-wall grid size (mm)	Maximum z^+
I	100 × 100	0.06	1.21
II	300 × 80	0.06	5.41
III	1,000 × 50	0.06	7.21
IV	1,000 × 30		
V	1,000 × 20		

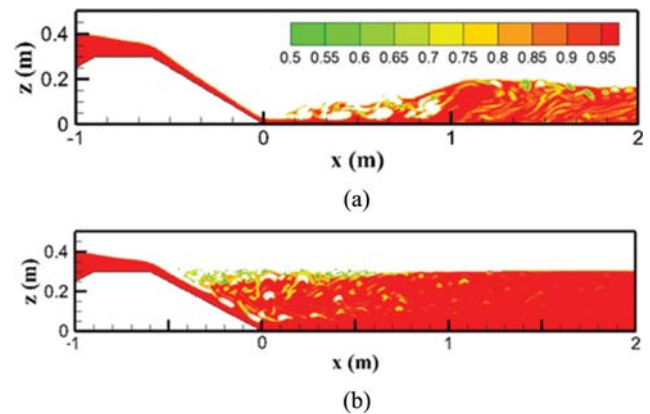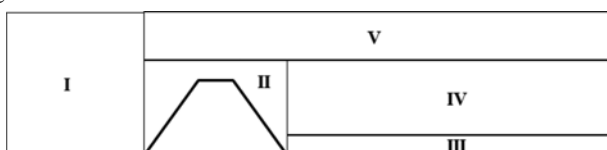*The computational domain is divided into 5 subdomains as given by the figure below.

Fig. 4. Contours of Ensemble-Averaged Volume Fraction of Water α, (a) For Free Jump, (b) For Submerged Jump ($S = 0.77$)

time step is updated automatically after each time step under the condition that the maximum Courant number would not exceed 0.5 to ensure the convergence and stability of the computations. After obtaining the converged solution, the mean variables are obtained by time-averaging for 20 s at a sampling rate of $\Delta t = 0.00005$ s.

4.3 Flow Structures

Figures 4(a) and 4(b) show the computed contours of the ensemble-averaged volume fraction of water α for the free jump and submerged jump for $S = 0.77$, respectively. The figures show contours of $\alpha > 0.5$, and $x = 0$ denotes the toe of the weir in the horizontal axis. As shown in the figures, complicated recirculations occur in the roller region for both jumps. For the free jump, the air entrained from the roller region is observed to affect the flow after the jump. For the submerged jump, the air is entrained at the plunging point and advects along the interface of the supercritical flow on the downslope of the weir, which appears obvious in the contour plot. In this case, the volume fraction is reduced immediately after plunging, leading to a decrease in buoyancy. This induces the adverse pressure gradient of the submerged jump, albeit of the nearly horizontal water surface in the recirculating region. This will be shown and discussed later in Figs. 8 and 12.

Figures 5(a) and 5(b) show the distributions of the streamwise mean velocity $\bar{u}$ at various longitudinal distances for the free jump and submerged jump for $S = 0.77$, respectively. In the figures, the computed results are compared with the measured data in Fritz and Hager (1998). The interface of the roller and the free surface are also plotted in the figures. In the simulated results, the interface of the roller is determined by the computed streamlines and the free surface by $\alpha = 0.5$. For both the free jump and submerged jump, the numerical model accurately predicts the two flow regimes that consist of recirculating flows over the wall-jet-like flow in the developed zone. The computed roller length for the submerged jump with $S = 0.77$ appears to be 2.2 times longer than that for the free jump. Compared with the velocity profile of the free jump, the velocity maximum for the submerged jump occurs in the vicinity quite close to the bed,
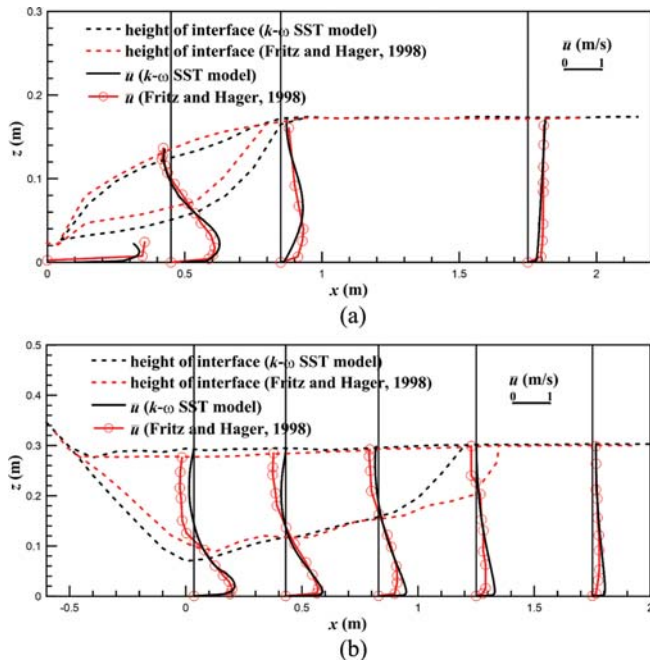
Fig. 5. Distribution of Streamwise Mean Velocity: (a) For Free Jump, (b) for Submerged Jump (S = 0.77)

resulting in a profile similar to that of the wall jet. This is because of the lower level of the adverse pressure gradient, which will be discussed quantitatively later in Fig. 12. The computed maximum backward velocity for the free jump is 1.67 times stronger than that for the submerged jump.

For the free jump in Fig. 5(a), the computed velocity profiles agree well with the measured data, but the computed roller length (L_r) appears to be slightly longer than the measured data. In detail, the computed value of $L_r/y_2 = 4.6$, which is 1.07 times larger than the measured value of 4.3 by Fritz and Hager (1998). For the free jump, the flow depth before the jump decreases slightly, like vena contracta, due to acceleration along the downslope of the weir (Gumus et al., 2016). Both the computed and measured velocity profiles in the developed zone indicate backward flows. The computed velocity profile at $x = 1.75$ m conforms well to the measured velocity profile, suggesting that the flow profile becomes that of a subcritical flow after the jump.

By contrast, for the submerged jump in Fig. 5(b), the computed recirculation region is observed to be slightly shorter than the

measured data in Fritz and Hager (1998). Specifically, the normalized roller lengths of L_r/y_2 for the computed results and measured data are 5.6 and 6.1, respectively. Regarding the velocity profile, the numerical model appears to accurately predict the features of the jet-like flow in the developed zone. However, the model under-predicts the backward flows near the free surface when compared with the measured data. This can be attributed to the computation of the velocity of the water-air mixture using the VOF method, as stated before. Similar to the free jump, the velocity profile at $x = 1.75$ m indicates that the flow becomes a normal subcritical flow after the jump.

Figure 6 shows the computed distributions of the x-component turbulence intensity u' at various longitudinal distances for the free jump and the submerged jump for $S = 0.77$. The turbulence intensity in the figure is normalized by the bulk velocity U_1, which is the approach velocity downstream of the toe of the weir for the free jump and upstream from the plunging point along the downslope for the submerged jumps. In the present study, the computed bulk velocities are 2.03 m s^{-1} for the free jump, and 1.69, 1.37, and 1.18 m s^{-1} for the submerged jumps of $S = 0.5$, 0.77, and 0.88, respectively. In the figure, the computed interface of the roller and the free surface are also plotted. It appears that the overall vertical structure of u' for the free jump is akin to that for the submerged jump. That is, in the developed zone, u' increases rapidly in the vicinity of the bed and shows the peak within the shear layer, located below the interface of the roller, decreasing slightly toward the free surface. For both the free jump and the submerged jump, the height of the maximum turbulence intensity is slightly higher than that of the maximum streamwise mean velocity, and the peak of u' is largest at the location where the developed zone starts, decreasing gradually with the longitudinal distance.

The distributions of the normalized Reynolds stress $-u'w'$ at various longitudinal distances for the free jump and the submerged jump for $S = 0.77$ are shown in Fig. 7. In the figure, the interface of the roller and free surface are plotted using dotted lines. The overall distribution of the Reynolds stress for the free jump is similar to that for the submerged jump. Specifically, the Reynolds stress is of a small positive value in the region very close to the bed, decreasing to a negative peak and increasing gradually thereafter. The heights of zero Reynolds stress near the bed and negative peak roughly correspond to the peak of the streamwise
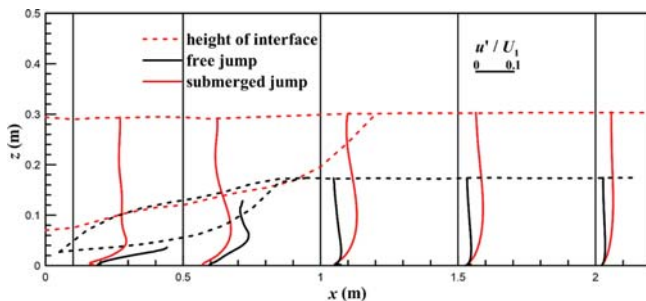

Fig. 6. Distribution of x-Component Turbulence Intensity
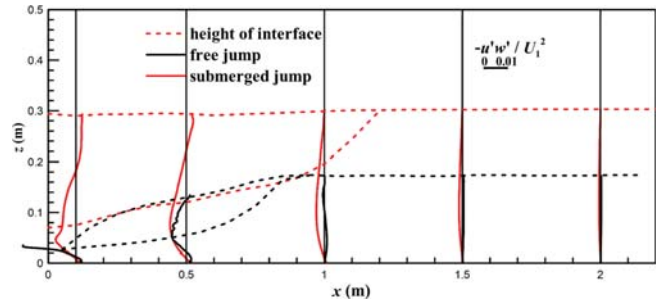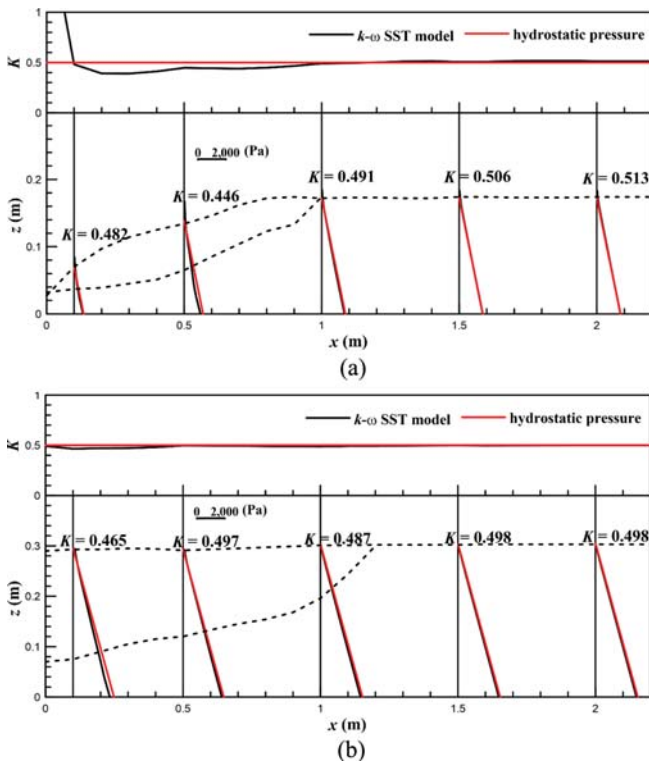

Fig. 7. Distribution of Reynolds Stress

Fig. 8. Distribution of the Mean Pressure: (a) For Free Jump, (b) For Submerged Jump (S = 0.77)

mean velocity and the inflection point of the mean velocity profile, respectively. The magnitude of the negative peak of the Reynolds stress is largest at the location where the jump starts and decreases in the longitudinal direction, resulting in the negative peak unidentifiable in the transition zone.

Figures 8(a) and 8(b) show the distributions of the mean pressure $\bar{p}$ at various longitudinal distances for the free jump and the submerged jump for $S = 0.77$, respectively. The hydrostatic pressure distribution is plotted for comparison. Also, shown in the figure is the distribution of the pressure correction factor K in Yen and Wenzel (1970) such as

$$K = \frac{\int \bar{p} dz}{\rho g y^2},$$ (11)

which is 0.5 for the hydrostatic pressure distribution. The mean pressure deviates from the hydrostatic pressure in the developed zone for both the free jump and the submerged jump. However, the deviation is much larger for the free jump. For the free jump, the pressure correction factor is very large at the toe of the weir ($x = 0$), which is due to the flow acceleration over the slope. The pressure correction factor decreases sharply for $0 < x < 0.1$ m and shows a minimum value of 0.39 at about $x = 0.2$ m. Then, the pressure correction factor increases gradually in the developed zone. The pressure becomes hydrostatic beyond the developed zone, namely $x > 1.0$ m. For the submerged jump for $S = 0.77$, the pressure coefficient decreases slightly, showing a minimum of 0.465 at about $x = 0.1$ m, and recovers to 0.5 from about $x = 0.5$ m.
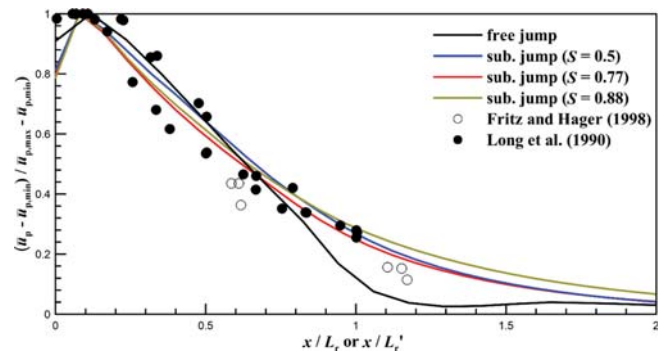

Fig. 9. Longitudinal Change in Peak Streamwise Mean Velocity

4.4 Longitudinal Change

Figure 9 shows the longitudinal decay of the peak streamwise mean velocity with distance for the free jump and submerged jumps. The vertical axis is normalized to make the maximum and minimum values of the peak streamwise mean velocities unity and zero, respectively. The horizontal axis is normalized by dividing x by the roller length for the free jump (L_r) and the roller length from the origin for the submerged jump (L_r). The measured data for the free jump (Fritz and Hager, 1998) and for the submerged jumps with $0.22 < S < 1.69$ (Long et al., 1990) are also plotted in the figure. Since Long et al.'s (1990) data are available only up to the developed zone, proper normalizations are made based on the computed results. Moderate agreement between the computed results and the measured data is observed in the figure. For both the free jump and the submerged jumps, the normalized peak velocity is maximum slightly downstream from the toe of the weir due to the vena contracta effect (Gumus et al., 2016). The normalized peak velocity for the free jump decays to 20% of the maximum in the developed zone, whereas the normalized peak velocity for the submerged jumps decays to about 27%. It is noteworthy that the normalized peak velocity for the free jump decays to nearly zero at $1.3L_r$ whereas that for the submerged jumps at $2.0L_r$'. Quantitatively, the decaying rates in the roller region are 2.47 m s⁻¹ m⁻¹ for the free jump, and 0.98, 0.76, and 0.63 m s⁻¹ m⁻¹ for submerged jumps of $S = 0.5$, 0.77, and 0.88, respectively.

The decay in the peak turbulence intensity with longitudinal distance is shown in Fig. 10 for the free jump and the submerged
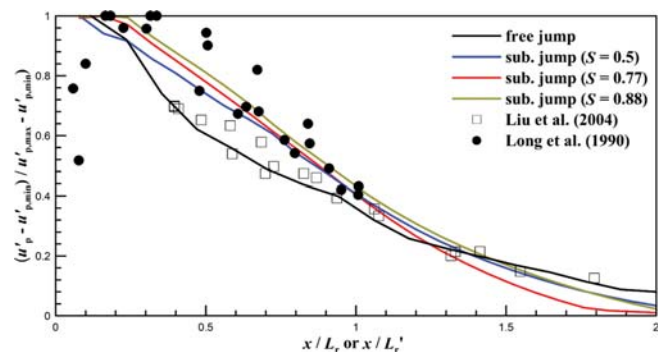

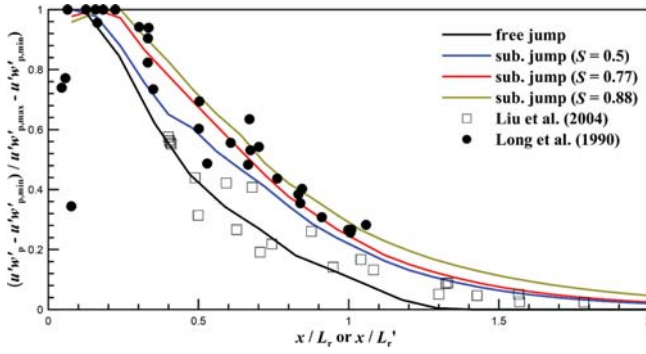**Fig. 10.** Longitudinal Change in Peak Turbulence Intensity

Fig. 11. Longitudinal Change in Peak Reynolds Stress

Fig. 12. Longitudinal Change in Mean Pressure at the Bed

jumps. The measured data for the free jump (Liu et al., 2004) and the submerged jump (Long et al., 1990) are also presented. Based on the computed results, adjustments are made in normalizing the measured data of Liu et al. (2004). Moderate agreement between the computed results and measured data is observed. For the free jump, the decay of the normalized peak turbulence intensity accelerates in the first half of the developed zone but decelerates in the second half. However, the normalized peak turbulence intensity for the submerged jumps decays linearly with the distance in the developed zone. As a result, the normalized peak turbulence intensity decays to 37% and 42% of their maximums at the end of the developed zone for the free jump and submerged jumps, respectively. The decaying rates of the submerged jumps in the roller region are 0.15, 0.10, and 0.09 m s^{-1} m^{-1} for submerged jumps of $S = 0.5$, 0.77, and 0.88, respectively.

Figure 11 shows the longitudinal decay of the peak Reynolds stress for the free jump and submerged jumps. Also presented are measured data for the free jump (Liu et al., 2004) and the submerged jump (Long et al., 1990). The computed results appear to be in good agreement with the measured data. Compared to the peak streamwise mean velocity and peak turbulence intensity, the peak Reynolds stress decays exponentially in the longitudinal direction. Further, the overall decaying pattern for the free jump is similar to that for the submerged jumps. However, the normalized peak Reynolds stress for the free jump decays faster than that for the submerged jumps. At the end of the developed zone, the free jump decays 88% of the peak Reynolds stress, but the submerged jumps 70 – 78% of the peak Reynolds stress depending on the submergence factor. Interestingly, the decaying of the peak Reynolds stress ends at $x/L_r = 1.3$ for the free jump but continues beyond $x/L_r' = 2.0$ for the submerged jumps. The decaying rates in the roller region are 0.04, 0.02, and 0.015 m^2 s^{-2} m^{-1} for submerged jumps of $S = 0.5$, 0.77, and 0.88, respectively.

Using Figs. 9 – 11, the similarities of decaying peak streamwise mean velocity, peak turbulence intensity, and peak Reynolds stress are investigated. As shown in Fig. 9, the decay of the peak streamwise mean velocity for the free jump appears to be similar to that for the submerged jumps for $x/L_r \leq 0.7$. However, for $x/L_r > 0.7$, the decay of the submerged jumps is retarded slightly, compared to that for the free jump. For the peak turbulence intensity in Figure 10, the decay of the free jump is accelerated
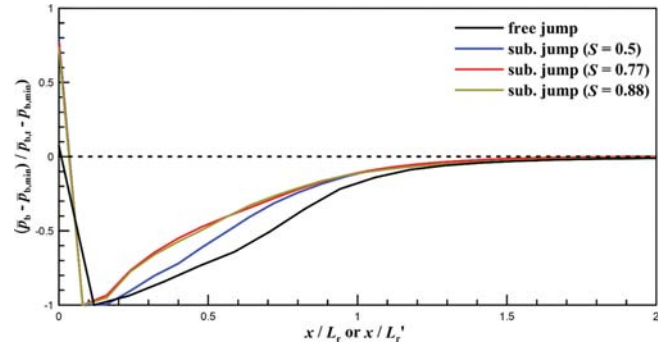
for $x/L_r \leq 0.5$ but is slowed down a little afterward, compared to the decay of the submerged jumps. As shown in Fig. 11, the decaying pattern of the peak Reynolds stress for the free jump is roughly similar to that for the submerged jumps. However, the decay for the free jump is faster and is completed at a distance slightly downstream from the roller region. In summary, the decays of the peak streamwise mean velocity, peak turbulence intensity, and peak Reynolds stress for the free jump are roughly similar to those for the submerged jumps. However, the decays of the submerged jumps are very similar regardless of the submergence factor. This is consistent with Fritz and Hager's (1998) finding that the peak streamwise mean velocity for both the free jump and the submerged jumps decay similarly.

4.5 Adverse Pressure Gradient and Energy Loss

The longitudinal distribution of the mean pressure at the bed is plotted in Fig. 12 for the free jump and the submerged jumps. The vertical axis is normalized to make the far downstream and minimum values of the mean pressure at the bed zero and minus unity, respectively. A general trend observed in the figure is that the mean pressure at the bed decreases sharply from the toe of the weir and increases gradually with the longitudinal distance. The sharp drop in the mean pressure at the bed results from the vena contracta effect. The mean pressure at the bed recovers slowly to that of the open-channel flow for the free jump. However, for the submerged jumps, recovery is faster. The negative pressure gradient of both the free jump and the submerged jumps is noteworthy in the figure. The adverse pressure gradient for the free jump can be attributed to both the inclined free surface and the change in the volume fraction of water in the developed zone, whereas the adverse pressure gradient for the submerged jump can only be ascribed to the change in the volume fraction of water since the free surface of the roller is nearly horizontal. For the submerged jumps, the values of the adverse pressure gradient are 0.26, 0.31, and 0.51 kPa m^{-1} for $S = 0.88$, 0.77, and 0.5, respectively, and the adverse pressure gradient is 1.11 kPa m^{-1} for the free jump. These values indicate that the adverse pressure gradient of the free jump is larger than that of the submerged jumps and that the adverse pressure gradient decreases as the submergence factor for the submerged jumps increases.

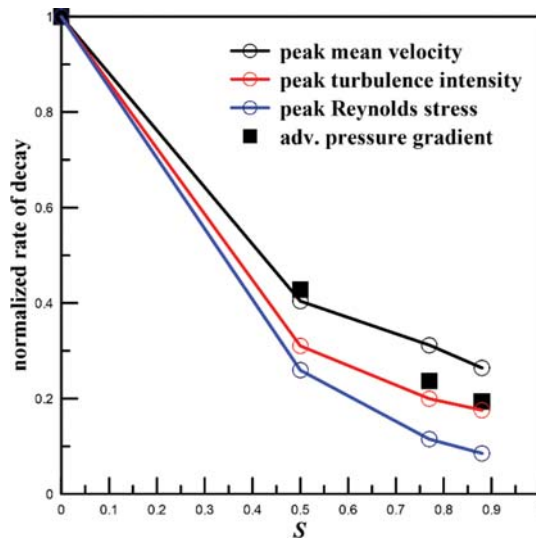Figure 13 shows the decaying rates of the peak streamwise

Fig. 13. Decaying Rate versus Submergence Factor

Fig. 14. Longitudinal Change in Energy Loss

the effect of the vena contracta. For submerged jumps, the head losses are 0.056, 0.032, and 0.027 m with $S = 0.5$, 0.77, and 0.88, respectively. They correspond to 43%, 25%, and 21% of the head loss by the free jump, respectively.

5. Conclusions

This study numerically investigated the longitudinal change in the flow structures and the loss of the kinetic energy for the free jump and submerged jumps of the flows over an embankment-type weir. The 2D URANS equations were solved with the k-ω SST turbulence model using the open source platform OpenFOAM. The free jump and submerged jumps were reproduced for the same unit discharge by varying the tailwater depth. The numerical model was validated by applying it to an experimental case of the free jump in the literature.

The longitudinal decays of the peaks of the streamwise mean velocity, turbulence intensity, and Reynolds stress were investigated. The decaying patterns of these flow structures for the free jump are roughly similar to those for the submerged jump. The normalized decaying rates of the peak mean velocity, peak turbulence intensity, and peak Reynolds stress were found to decrease with the submergence factor. The drop in decaying rates from the free jump to the submerged jumps appeared to be substantial. The ratio of the decaying rates for the free jump to that for the submerged jump with $S = 0.5$ ranges between 0.6 for the mean velocity and 0.77 for the peak Reynolds stress. The faster decay of the peak Reynolds stress for the free jump is due to the extinction of the shear layer between the wall-jet region and the roller region. Noticeably, the change in the adverse pressure gradient agrees well with that of the decaying rates. This suggests that the adverse pressure gradient plays a key role in the longitudinal decay of the mean flow and turbulence statistics for both the free jump and the submerged jumps. The decaying rate decreases almost linearly for the submerged jumps with an increasing submergence factor.

Finally, the longitudinal distribution of the energy loss was presented. For both the free jump and the submerged jumps, the dissipation of the mean kinetic energy is nearly terminated within the developed zone. The energy loss for the free jump is larger than that for the submerged jumps, and the energy loss for

mean velocity, peak turbulence intensity, and peak Reynolds stress with the submergence factor for both the free jump and the submerged jumps. Here, it is assumed that the decay in the Reynolds stress is approximated by a straight line. The figure also plots the magnitude of the adverse pressure gradient. In the figure, the submergence factor of zero denotes the free jump, with the vertical axis normalized by the values for the free jump. The decaying rates drop substantially from the free jump to the submerged jumps. The drop in the decaying rate of the peak mean velocity for the submerged jump with $S = 0.5$ is about 60% of the decaying rate for the free jump, which is the least value, whereas the drop in the peak Reynolds stress is about 77%, which is the largest value. Interestingly, the changes in the mean flow and turbulence statistics with S agree well with the change in the adverse pressure gradient. This implies that the adverse pressure gradient plays a key role in the longitudinal decay of these variables, as can be deduced from Eqs. (1) and (2). The decaying rate for the submerged jumps appears to decrease almost linearly with the submergence factor. For the submerged jumps, the decaying rate of the peak mean velocity is highest, followed by the peak turbulence intensity and peak Reynolds stress.

The change in the energy loss with distance is presented in Fig. 14 for the free jump and submerged jumps. Here, the energy loss is calculated by comparing the specific energy before the jump with that at a particular distance. In the roller region, the volume fraction of water is considered to compute the flow depth, and the backward velocity is ignored. The energy correction factors for both the free jump and the submerged jumps range between 1.0 and 1.8. For both the free jump and the submerged jumps, a general trend observed in the figure is that the head loss increases with the distance in the developed zone and shows the maximum at about the end of the developed zone. The head loss then becomes more or less constant. The head loss for the free jump is 0.129 m, which is slightly larger than 0.116 m obtained from the Belanger equation. This difference can be attributed to
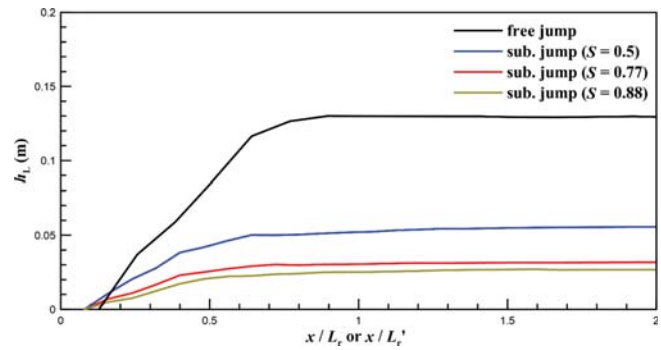
the submerged jumps increases with a decreasing submergence factor. Interestingly, it was observed that for both the free jump and the submerged jumps, the decay of the flow structures continues beyond the developed zone. This is due to that the shear layer disappears at the end of the developed zone, resulting in the whole restructuring of the mean flow and turbulence structures to those of the ordinary open-channel flow. This restructuring proceeds in the transition zone without spending too much mean kinetic energy.

Acknowledgments

ORCID

Sung-Uk Choi ⓘ https://orcid.org/0000-0002-0802-7705

References

Chow VT (1959) Open channel hydraulics. McGraw-Hill, New York

Fritz HM, Hager WH (1998) Hydraulics of embankment weirs. *Journal of Hydraulic Engineering* 124(9):963-971, DOI: 10.1061/(ASCE)0733-9429(1998)124:9(963)

Gumus V, Simsek O, Soydan NG, Akoz MS, Kirkgoz MS (2016) Numerical modeling of submerged hydraulic jump from a sluice gate. *Journal of Irrigation and Drainage Engineering* 142(1):04015037, DOI: 10.1061/(ASCE)IR.1943-4774.0000948

Hager WH (1992) Energy dissipators and hydraulic jump. Water science of technology library, Volume 8, Kluwer, Dordrecht, Netherlands, 67-75, DOI: 10.1007/978-94-015-8048-9

Harada S, Li SS (2018) Modelling hydraulic jump using the bubbly two-phase flow method. *Environmental Fluid Mechanics* 18:335-356, DOI: 10.1007/s10652-017-9549-5

Hirt CW, Nichols BD (1981) Volume of fluid (VOF) method for the dynamics of free boundaries. *Journal of Computational Physics* 39(1):201-225, DOI: 10.1016/0021-9991(81)90145-5

Jasak H (2009) OpenFOAM: Open source CFD in research and industry. *International Journal of Naval Architecture and Ocean Engineering* 1(2):88-94, DOI: 10.2478/IJNAOE-2013-0011

Javan M, Eghbalzadeh A (2013) 2D numerical simulation of submerged hydraulic jumps. *Applied Mathematical Modelling* 37(10-11):6661-6669, DOI: 10.1016/j.apm.2012.12.016

Jesudhas V, Balachandar R, Roussinova V, Barron R (2018) Turbulence characteristics of classical hydraulic jump using DES. *Journal of Hydraulic Engineering* 144(6):04018022, DOI: 10.1061/(ASCE)HY.1943-7900.0001427

Jesudhas V, Roussinova V, Balachandar R, Barron R (2017) Submerged hydraulic jump study using DES. *Journal of Hydraulic Engineering* 143(3):04016091, DOI: 10.1061/(ASCE)HY.1943-7900.0001231

Kang S, Lightbody A, Hill C, Sotiropoulos F (2011) High-resolution numerical simulation of turbulence in natural waterways. *Advances in Water Resources* 34(1):98-113, DOI: 10.1016/j.advwatres.2010.09.018

Khosronejad A, Kozarek JL, Palmsten ML, Sotiropoulos F (2015) Numerical simulation of large dunes in meandering streams and rivers with in-stream rock structures. *Advances in Water Resources* 81:45-61, DOI: 10.1016/j.advwatres.2014.09.007

Lin C, Hsieh SC, Lin IJ, Chang KA, Raikar RV (2012) Flow property and self-similarity in steady hydraulic jumps. *Experiments in Fluids* 53(5):1591-1616, DOI: 10.1007/s00348-012-1377-2

Liu M, Rajaratnam N, Zhu DZ (2004) Turbulence structure of hydraulic jumps of low Froude numbers. *Journal of Hydraulic Engineering* 130(6):511-520, DOI: 10.1061/(ASCE)0733-9429(2004)130:6(511)

Long D, Steffler PM, Rajaratnam N (1990) LDA study of flow structure in submerged hydraulic jump *Journal of Hydraulic Research* 28(4):437-460, DOI: 10.1080/00221689009499059

Long D, Steffler PM, Rajaratnam N (1991) A numerical study of submerged hydraulic jumps. *Journal of Hydraulic Research* 29(3):293-308, DOI: 10.1080/00221689109498435

Menter FR (1992) Improved two-equation k-omega turbulence models for aerodynamic flows. NASA Ames Research Center, Moffett Field, CA

Narasimhan S, Bhargava VP (1976) Pressure fluctuations in submerged jump. *Journal of the Hydraulics Division* 102(3):339-350, DOI: 10.1061/JYCEAJ.0004490

Paik J, Eghbalzadeh A, Sotiropoulos F (2009) Three-dimensional unsteady RANS modeling of discontinuous gravity currents in rectangular domains. *Journal of Hydraulic Engineering* 135(6):505, DOI: 10.1061/(ASCE)HY.1943-7900.0000034

Pourabdollah N, Heidarpour M, Abedi Koupai J (2020) Characteristics of free and submerged hydraulic jumps in different stilling basins. *Proceedings of the Institution of Civil Engineers-Water Management* 173(3):121-131, DOI: 10.1680/jwama.19.00029

Wang H, Chanson H (2015) Experimental study of turbulent fluctuations in hydraulic jumps. *Journal of Hydraulic Engineering* 141(7):04015010, DOI: 10.1061/(ASCE)HY.1943-7900.0001010

Wang H, Felder S, Chanson H (2014) An experimental study of turbulent two-phase flow in hydraulic jumps and application of a triple decomposition technique. *Experiments in Fluids* 55(7):1-18, DOI: 10.1007/s00348-014-1775-8

Wu S, Rajaratnam N (1995) Free jumps, submerged jumps and wall jets. *Journal of Hydraulic Research* 33(2):197-212, DOI: 10.1080/00221689509498670

Wu S, Rajaratnam N (1996) Transition from hydraulic jump to open channel flow. *Journal of Hydraulic Engineering* 122(9):526-528, DOI: 10.1061/(ASCE)0733-9429(1996)122:9(526)

Yen BC, Wenzel HG (1970) Dynamic equations for steady spatially varied flow. *Journal of the Hydraulics Division* 96(3):801-814, DOI: 10.1061/JYCEAJ.0002380